

The peculiar hard state behaviour of the black hole X-ray binary Swift J1727.8–1613

A. K. Hughes,¹★ F. Carotenuto,² T. D. Russell,³ A. J. Tetarenko,⁴ J. C. A. Miller-Jones,⁵ R. M. Plotkin,^{6,7} A. Bahramian,⁵ J. S. Bright,^{1,8} F. J. Cowie,¹ J. Crook-Mansour,¹ R. Fender,^{1,9} J. K. Khavulsay,¹⁰ A. Kirby,⁵ S. Jones,⁵ M. McCollough,¹¹ R. Rao,¹¹ G. R. Sivakoff,¹² S. D. Vrtilek,¹¹ D. R. A. Williams-Baldwin,¹³ C. M. Wood,⁵ D. Altamirano,¹⁴ P. Casella,² N. Castro Segura,¹⁵ S. Corbel,¹⁶ M. Del Santo,³ C. Echiburú-Trujillo,¹⁷ J. van den Eijnden,^{15,18} E. Gallo,¹⁹ P. Gandhi,¹⁴ K. I. I. Koljonen,²⁰ T. Maccarone,²¹ S. B. Markoff,^{18,22} S. Motta,^{1,23} D. M. Russell,²⁴ P. Saikia,²⁴ A. W. Shaw,²⁵ R. Soria,^{26,27} J. A. Tomsick,²⁸ W. Yu,^{29,30} X. Zhang³⁰

Affiliations are listed at the end of the paper

Accepted XXX. Received YYY; in original form ZZZ

ABSTRACT

Tracking the correlation between radio and X-ray luminosities during black hole X-ray binary outbursts is a key diagnostic of the coupling between accretion inflows (traced by X-rays) and relativistic jet outflows (traced by radio). We present the radio–X-ray correlation of the black hole low-mass X-ray binary Swift J1727.8–1613 during its 2023–2024 outburst. Our observations span a broad dynamic range, covering ~ 4 orders of magnitude in radio luminosity and ~ 6.5 in X-ray luminosity. This source follows an unusually radio-quiet track, exhibiting significantly lower radio luminosities at a given X-ray luminosity than both the standard (radio-loud) track and most previously known radio-quiet systems. Across most of the considered distance range ($D \sim 1.5$ – 4.3 kpc), Swift J1727.8–1613 appears to be the most radio-quiet black hole binary identified to date. For distances ≥ 4 kpc, while Swift J1727 becomes comparable to one other extremely radio-quiet system, its peak X-ray luminosity ($\geq 5 \times 10^{38} \text{ erg s}^{-1}$) exceeds that of any previously reported hard-state black hole low-mass X-ray binary, emphasising the extremity of this outburst. Additionally, for the first time in a radio-quiet system, we identify the onset of X-ray spectral softening to coincide with a change in trajectory through the radio–X-ray plane. We assess several proposed explanations for radio-quiet behaviour in black hole systems in light of this dataset. As with other such sources, however, no single mechanism fully accounts for the observed properties, highlighting the importance of regular monitoring and the value of comprehensive (quasi-)simultaneous datasets.

Key words: accretion, accretion discs — black hole physics — ISM: jets and outflows — radio continuum: stars — stars: individual Swift J1727.8–1613 — X-rays: binaries

1 INTRODUCTION

A black hole (BH) low-mass X-ray binary (LMXB) is an accreting binary system in which a stellar-mass black hole (typically $\sim 7 M_{\odot}$; Corral-Santana et al. 2016) accretes material from a low-mass donor star ($\lesssim 1 M_{\odot}$). As in other accretion-powered systems (Livio 2002), the accretion process in BH LMXBs gives rise to highly collimated, relativistic outflows, referred to as *jets*. In these systems, the accretion flow is primarily traced by X-ray emission and the jets are most commonly observed at radio frequencies. Although a robust empirical connection has been established between accretion states and jet activity, the physical mechanisms governing the accretion–ejection coupling remain poorly understood.

BH LMXBs spend the majority of their lifetimes in quiescence at an undetected or low X-ray luminosity ($L_X < 10^{34} \text{ erg s}^{-1}$; Plotkin et al. 2013). As a result, these systems are primarily discovered

during their bright active states (‘outbursts’) during which their X-ray luminosities can reach values $\geq 10^{38} \text{ erg s}^{-1}$. In outburst, the system evolves through ‘accretion states’, which are defined by the X-ray spectral and timing properties; the two canonical accretion states being the *hard* and *soft* state (see, e.g., McClintock & Remillard 2006; Kalemci et al. 2022; De Marco et al. 2022, for reviews).

In the hard state, the X-ray spectrum is dominated by X-ray photons that have been Compton up-scattered in a coronal flow (Thorne & Price 1975; Shapiro et al. 1976), with sub-dominant contributions from an accretion disc (Done et al. 2007). In contrast, the soft state exhibits an inversion of the dominant X-ray component, with the thermalised (multi-colour) accretion disc becoming dominant. An outburst typically begins in the hard state, with rising X-ray luminosity, transitions to the soft state near peak brightness, and returns to the hard state during the decay phase. During transitions, BH LMXBs exhibit intermediate X-ray properties: the hard-intermediate and soft-intermediate states (Belloni & Motta 2016). While a hard→soft→hard evolution is considered typical, some out-

★ E-mail: hughesakh@gmail.com

bursts display repeated transitions through the intermediate state before reaching the soft state, or only remain in a hard state (Brocksopp et al. 2001; Tetarenko et al. 2016; Alabarta et al. 2021).

Jets from BH LMXBs are broadly classified as either continuously accelerated, steady ‘compact jets’ or transient ‘jet ejecta’ (see, e.g., Fender et al. 2004; Fender 2006, for reviews). The type of jet produced and the observed radio properties correlate with the accretion state. Compact jets are associated with the hard (and perhaps, hard-intermediate) states. Their emission is consistent with a partially self-absorbed synchrotron spectrum, often exhibiting a flat or mildly inverted spectral index ($\alpha \gtrsim 0$; where the flux density, $F_{R,\nu}$, scales with the observing frequency, ν , as $F_{R,\nu} \propto \nu^\alpha$).

In the soft state, the compact jet emission is quenched (e.g., Tananbaum et al. 1972; Fender et al. 1999b; Coriat et al. 2011; Russell et al. 2011, 2019a; Maccarone et al. 2020). However, one or more transient jets may be launched during the hard→soft transition (e.g. Mirabel & Rodríguez 1994; Fender et al. 1999a; Brocksopp et al. 2002; Russell et al. 2019b; Bright et al. 2020; Carotenuto et al. 2021a; Wood et al. 2021). Transient jets are discrete, optically thin ($\alpha \lesssim -0.6$) knots of synchrotron-emitting plasma launched from the system at mildly to highly relativistic speeds, decoupled from the accretion flow.

The radio luminosity of compact jets (L_R) exhibits a positive, non-linear correlation with the X-ray luminosity (L_X), providing evidence for a coupling between accretion and jet production. This L_R – L_X relation extends across several orders of magnitude in luminosity (e.g. Hannikainen et al. 1998; Corbel et al. 2003; Gallo et al. 2003, 2004; Corbel et al. 2013a), and was initially thought to follow a single power-law relation, $L_X \propto L_R^\beta$, with $\beta \sim 0.6$ —the so-called ‘standard track’ (Gallo et al. 2003). With the inclusion of a mass dependence, this relation could be extrapolated to accreting supermassive black holes (i.e., Active Galactic Nuclei; AGN), suggesting a universal scaling (e.g., ‘the fundamental plane of black hole activity’; Merloni et al. 2003).

However, it was later discovered that some BH LMXBs display significantly lower radio luminosities at a given L_X (e.g., H1743–32; Jonker et al. 2010; Coriat et al. 2011; Williams et al. 2020). A broken power law better describes these ‘outlier’ sources—referred to as the ‘hybrid track’—featuring a steep branch ($\beta \gtrsim 1$) at high X-ray luminosities ($L_{X,\text{tran}} \gtrsim 10^{36} \text{ erg s}^{-1}$), which transitions to a shallow branch ($\beta \lesssim 0.3$) that rejoins the standard track ($\beta \sim 0.6$) at lower luminosities. The X-ray luminosity at which outliers reconnect with the standard track is typically around $\sim 10^{35} \text{ erg s}^{-1}$ and a radio luminosity of $\sim 10^{29} \text{ erg s}^{-1}$ (e.g. Coriat et al. 2011; Plotkin et al. 2017b), although some sources rejoin the standard track at significantly lower (e.g., Carotenuto et al. 2021b) or higher luminosities (e.g., Islam & Zdziarski 2018; Koljonen & Russell 2019). Notably, although termed ‘outliers’, more systems have been observed to follow the hybrid track than the standard track (e.g., Gallo et al. 2018).

The outliers led to the introduction of ‘radio-loud’ (i.e., standard-track) and ‘radio-quiet’ nomenclature, implicitly treating the standard-track and outlier sources as two distinct populations. It should be noted that ‘radio-quiet’ does not comment on the physical origin of the different populations; it simply means that some sources have lower radio luminosities at a given X-ray luminosity. The reason for the difference may, as some authors have proposed, be due to enhanced X-ray emission from the accretion flow (‘X-ray-bright’) rather than suppressed radio emission from the jet (e.g., Xie & Yuan 2012; Meyer-Hofmeister & Meyer 2014; Xie & Yuan 2016). Moreover, the apparent dichotomy may not reflect two distinct sub-populations (Gallo et al. 2014, 2018); instead, the allowable L_R – L_X tracks may span the full luminosity range, from the standard track (or above) to extremely radio-quiet behavior, depending on source

properties. The physical mechanisms responsible for the radio-loud and radio-quiet sources—whether arising from variations in the jet, the accretion flow, or both (e.g., Coriat et al. 2011; Espinasse & Fender 2018)—remain poorly understood. It is also unclear whether individual sources are intrinsically tied to one track or can transition between radio-loud and radio-quiet behaviour across different outbursts or spectral states, highlighting the need for continued monitoring to disentangle the nature of these ‘populations’.

1.1 The Black Hole Low-Mass X-ray Binary Swift J1727.8–1613

Swift J1727.8–1613 (hereafter Swift J1727) is a BH LMXB that was discovered in August 2023 during its first recorded outburst. The event lasted approximately one year and was the subject of intensive observational campaigns, particularly at radio and X-ray frequencies (e.g., Bollemeijer et al. 2023a,b; Miller-Jones et al. 2023a,b; Ingram et al. 2023; Peng et al. 2024; Liu et al. 2024; Wood et al. 2025), making it an excellent candidate to augment our current L_R – L_X catalogues. Swift J1727 swiftly became one of the brightest X-ray sources in the sky (e.g. Page et al. 2023; Kennea & Swift Team 2023), though it remains unclear whether this brightness is intrinsic or due to its proximity.

Mata Sánchez et al. (2024, 2025) presented optical observations of Swift J1727, measuring its radial velocity and dynamically confirming the presence of a black hole ($M_{\text{BH}} > 3 M_\odot$). Furthermore, these authors estimated a distance of $3.7 \pm 0.3 \text{ kpc}$ using an empirical relation between binary period (P_{orb} of 10.8 h) and absolute r -band magnitude, together with pre-outburst photometry and optical extinction estimates. Burridge et al. (2025) reanalysed these data and supplemented them with near-UV spectra, reporting an updated distance of $5.5^{+1.5}_{-1.1} \text{ kpc}$. However, most recently, Burridge et al. (private communication) have revised this estimate to $2.6^{+1.7}_{-1.1} \text{ kpc}$, incorporating updated properties of the companion star. Our analysis adopts the most recent inferred distance range of 1.5–4.3 kpc, corresponding to the 68% equal-tailed interval. The estimate reported by Mata Sánchez et al. (2025) lies well within this range. We note that distances outside this interval would only make the source appear more extreme, and therefore do not contradict our conclusions.

In this paper, we utilise the comprehensive radio light curves presented in Hughes et al. (submitted), alongside quasi-simultaneous X-ray observations, to investigate the L_R – L_X evolution of Swift J1727 and the connection between its accretion flow and compact jets. In Section 2, we describe the radio and X-ray data selection and analysis. Section 3 presents the L_R – L_X track, and in Section 4 we discuss the physical interpretations.

2 OBSERVATIONS AND METHODS

This section summarises the observations and analysis used to produce the final data products, all of which—including raw and processed data and analysis scripts—are available on GitHub¹. While Swift J1727 underwent multiple state transitions near the outburst peak (e.g., Yu 2023), we focus only on the hard states immediately following the outburst rise (henceforth ‘the rise hard state’) and during the decay (‘the decay hard state’) due to the complex radio behavior and jet ejecta contributions during intermediate phases (see Figure A1).

¹ https://github.com/AKHughes1994/SwJ1727_2023_Outburst

2.1 Radio Observations

Swift J1727 was the focus of multiple extensive radio campaigns, which were compiled and presented in Hughes et al. (submitted). In this work, we use a subset of those data, obtained with MeerKAT, the Karl G. Jansky Very Large Array (VLA), and the Australia Telescope Compact Array (ATCA), as these instruments captured both the rise and decay hard states.

The L_R – L_X relation pertains specifically to compact jet emission during the hard state. Accordingly, during the rising hard state, we include only those observations taken before the onset of radio flaring (which began on 2023 September 19; MJD 60206), after which observations with the Very Long Baseline Array revealed that the flares coincided with transient jet ejections (Wood et al. 2025). Hughes et al. (submitted) presented the entire radio light curve of Swift J1727, providing the integrated flux densities, which—during most of the decay hard state—included both unresolved emission from the compact jet (reappearing at the ‘core’ position) and spatially resolved jet ejecta (see Figure A2). The angular extent of (detectable) emission regions from the compact jet is $\sim 0.040''$ (Wood et al. 2024), rendering it unresolved at the angular resolution of MeerKAT, the VLA, and ATCA ($\gtrsim 1''$); we measure the compact jet’s flux density by fitting only the core emission.

However, throughout the soft state, steep-spectrum (and fading) radio emission was detected at the core position. Since compact jet emission is quenched by $\gtrsim 3$ orders of magnitude in the soft state and, when detected in the hard state, exhibits a flat radio spectrum, this steep-spectrum component most likely originates from long-lived transient jet(s) that remain unresolved from the radio core (similar to those seen in MAXI J1535–571; Russell et al. 2019b). As a result, following the re-brightening of the compact jet during the decay hard state, the core emission is a superposition of compact jet and ejecta emission. To account for ejecta contributions, we modelled the fading steep-spectrum component with an exponential decay². Extrapolating this decay to the hard state epochs—and accounting for spectral indices—we subtracted the modelled value from the observed core flux density, adopting the resulting value as the true compact jet flux density (see Appendix B).

We included a systematic error equal to 10% of the measured flux density (added in quadrature) as fractional errors are often recommended to account for the secular evolution of the calibrator(s) (e.g., 3% for ATCA; Massardi et al. 2011; McConnell et al. 2012). While 10% is overly conservative when considering calibration systematics alone, it should implicitly account for additional systematics from interpolation errors or imperfect subtraction of the decay.

2.2 X-ray Observations

Swift J1727 was monitored with the X-ray Telescope onboard the Neil Gehrels Swift Observatory (Swift-XRT; Burrows et al. 2005). We include 20 observations from the rise hard state (2023 Aug 28–Sep 20; MJD 60184–60207, target ID: 1186959³), and 22 from the decay hard state (2024 Feb 03–Jun 03; MJD 60343–60464, target IDs: 16584, 89766). Spectra were extracted using the SWIFTTOOLS pipeline (Evans et al. 2007, 2009) and analysed in XSPEC (Arnaud 1996).

Pile-up becomes significant for $\gtrsim 150$ counts s^{-1} , and the pipeline includes standard corrections that are generally effective. However,

due to its extreme brightness ($\gtrsim 5000$ counts s^{-1}), the rise hard state data lie in a poorly calibrated regime (P. Evans, private communication). Consequently, we applied a 10% systematic flux error, added in quadrature with statistical uncertainties; we conservatively apply this to all X-ray epochs, even those unaffected by pile-up.

For spectra with ≥ 500 counts, we binned into 25-count intervals (≥ 20 bins) and fit using χ^2 statistics with an absorbed power law plus disc blackbody model: `tbabs * (pegpwrlw + diskbb)`, capturing both coronal and disc emission. Absorption was modelled with `tbabs`, adopting Wilms et al. (2000) abundances. After fitting, we measured unabsorbed 1–10 keV flux with the convolution model `cflux` (i.e., `tbabs * cflux * (pegpwrlw + diskbb)`). We initially let N_H vary, obtaining a variance-weighted average of $(2.68 \pm 0.02) \times 10^{21} \text{ cm}^{-2}$ consistent with past measurements (e.g., O’Connor et al. 2023; Draghis et al. 2023; Peng et al. 2024; Stiele & Kong 2024), and then fixed $N_H \equiv 2.68 \times 10^{21} \text{ cm}^{-2}$ for final fits. For spectra with fewer than 500 counts, we used `cstat` fitting (Cash 1979) with single-count binning. In cases where `cstat` was applied, or when χ^2 -binned epochs included fewer than 50 bins, we adopted a simplified power law model: `tbabs*pegpwrlw`, with fixed N_H .

Given the quasi-simultaneity of X-ray and radio data (typically $\lesssim 3$ days apart), we linearly interpolated the X-ray flux (in log-space) to the radio observation epochs. Although approximate, this approach captures the evolution of Swift J1727 (see Figures A3 and A4).

2.3 Luminosity Conversion

As is standard in L_R – L_X analyses (e.g., Bahramian & Rushton 2022), we calculate the 1–10 keV X-ray luminosities (L_X) and 5 GHz radio luminosities (L_R) from the unabsorbed X-ray flux (F_X) and radio flux density ($F_{R,\nu}$), using $L_X = 4\pi D^2 F_X$ and $L_R = 4\pi D^2 \nu_0 F_{R,\nu_0}$, where $\nu_0 = 5$ GHz. Since our observations span 0.3–15 GHz, we scale the flux density measured at the observing frequency ν using the spectral index α : $F_{\nu_0} = F_{\nu}(\nu_0/\nu)^\alpha$. These luminosities form the basis of the radio–X-ray correlation shown in Figure 1.

Many of the radio epochs include simultaneous multi-frequency coverage. When available, we selected the flux density closest in frequency to 5 GHz. To account for spectral evolution, we calculate inter-band spectral indices from the multi-frequency data. However, most observations during the decay phase were single-frequency. To avoid systematic biases associated with intra-band spectral indices—such as the artificial spectral ‘flattening’ seen in $<30\sigma$ VLA detections (e.g. Heywood et al. 2016)—we interpolate the 1.28 GHz MeerKAT data to match the ATCA and VLA observation times. This approach allows us to estimate inter-band spectral indices from the interpolated flux densities. For the ATCA observations, which were recorded simultaneously at 5.5 and 9 GHz, we verified the accuracy of the interpolated spectral index by comparing it with the ATCA-only inter-band spectral index and found good agreement (see Figure 2, second panel, star markers). We then used the ensemble of inter-band spectral indices to scale all radio flux densities to 5 GHz, adopting the spectral index measurement closest in time to each corresponding flux density. We include the final L_R – L_X values in Table C1.

3 RESULTS

In Figure 1, we present the L_R – L_X evolution of Swift J1727. Due to uncertainties in its distance, we plot three curves assuming distances of 1.5, 2.6, and 4.3 kpc. For context, we include an archival sample (grey circles; Bahramian & Rushton 2022), highlighting the

² A power law model was also fit to the decay; however, given the magnitude of the measurement errors, its fit was indistinguishable from the exponential.

³ Labelled as GRB 230824A in the Swift-XRT archive due to initial misidentification as a gamma-ray burst.

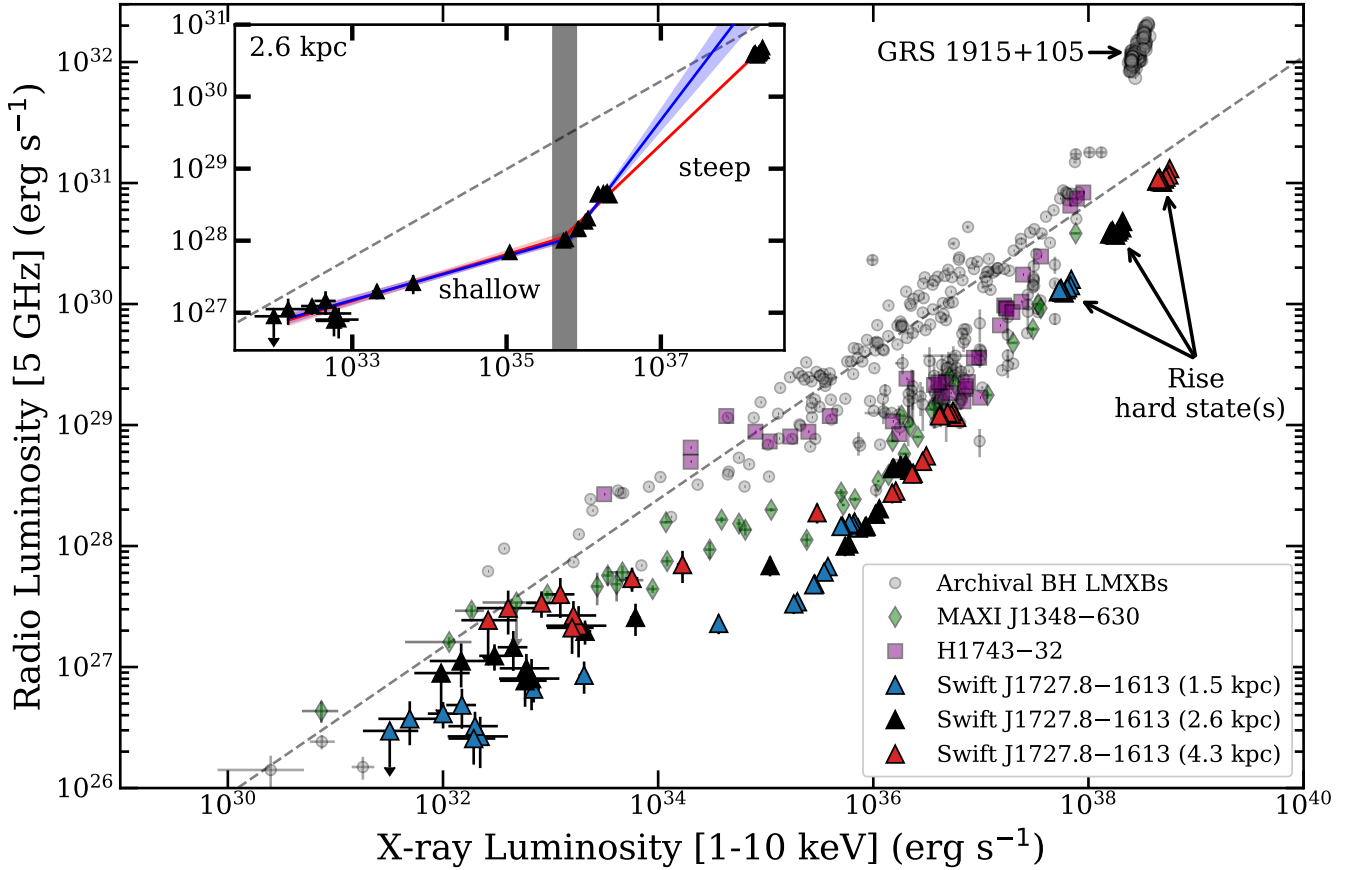


Figure 1. The L_R – L_X evolution of Swift J1727 (triangles) is shown alongside archival BH LMXBs (grey circles; Bahramian & Rushton 2022), with H1743–322 (purple squares) and MAXI J1348–630 (green diamonds) highlighted for comparison. The inset shows a broken power-law fit ($D=2.6$ kpc): red for all data, blue for the decay hard state. The grey shaded region marks the (approximate) 1σ range of the transitional luminosity ($L_{X,\text{tran}}$). The Swift J1727 observations in the upper right-hand corner correspond to the rising hard states. Swift J1727’s hybrid track is either an unusually faint decay or an unusually bright peak luminosity in the hard state, depending on the distance.

archetypal radio-quiet source H1743–32 (blue squares; Coriat et al. 2011), as well as MAXI J1348–630—which underwent the most radio-quiet evolution of all archival sources to date (green diamonds; Carotenuto et al. 2021b; Carotenuto et al. 2022).

The L_R – L_X evolution reveals that its radio–X-ray correlation cannot be adequately described by a single power law of the form $L_R \propto L_X^\beta$, as is typical for radio-quiet systems. Following the methodology applied to other radio-quiet sources (e.g. Coriat et al. 2011; Carotenuto et al. 2021b), we therefore model the evolution with a broken power law in logarithmic space:

$$L_R \propto \begin{cases} (L_X/L_{X,\text{tran}})^{\beta_{\text{shallow}}}, & \text{if } L_X < L_{X,\text{tran}} \\ (L_X/L_{X,\text{tran}})^{\beta_{\text{steep}}}, & \text{if } L_X \geq L_{X,\text{tran}} \end{cases} \quad (1)$$

accounting for uncertainties in both L_R and L_X using the odr function from the PYTHON package SCIPY.

As our monitoring spans both the rise and decay hard states, we fit the L_R – L_X data under two scenarios (adopting $D = 2.6$ kpc): (i) using both outburst phases, and (ii) using only the decay data, which captures both the steep and shallow tracks (see inset of Figure 1). In both cases, the shallow track is robustly constrained and in strong agreement yielding $\beta_{\text{shallow}} = 0.30 \pm 0.02$ for (i) and 0.32 ± 0.03 for (ii), which is unsurprising, given that shallow track occurs only during the decaying hard state. The transition lumi-

nosities are similarly consistent within uncertainties, with $L_{X,\text{tran}} = (7.1 \pm 0.9) \times 10^{35} \text{ erg s}^{-1}$ for (i), and $(5.4 \pm 1.1) \times 10^{35} \text{ erg s}^{-1}$ for (ii). The power law indices are agnostic of source distance whereas the luminosities—both at the transition to the shallow track ($L_{X,\text{tran}}$) and when rejoining the standard track ($L_{X,\text{rejoin}}$)—scale with distance as $L_{X,\text{tran}} \approx 6 \times 10^{35} (D/2.6 \text{ kpc})^2 \text{ erg s}^{-1}$ and $L_{X,\text{rejoin}} \approx 10^{32} (D/2.6 \text{ kpc})^2 \text{ erg s}^{-1}$, respectively.

As expected, a modest discrepancy ($\lesssim 2.7\sigma$) emerges between the steep-track indices, driven by the rising hard state being clustered at luminosities $\gtrsim 4$ orders of magnitude higher than those observed during the decay. Specifically, we measure $\beta_{\text{steep}} = 1.02 \pm 0.01$ for the full dataset and $\beta_{\text{steep}} = 1.42 \pm 0.15$ when fitting the decay phase alone. While this difference is $< 3\sigma$, it may hint at mild evolution in the L_R – L_X relation, consistent with prior studies showing limited variability in slope over narrow luminosity ranges (Corbel et al. 2013a). The tendency for BH LMXBs to appear fainter in radio during the rising hard state may also contribute to the shallower slope when rise data are included (Corbel et al. 2013a; Islam & Zdziarski 2018). Nevertheless, the two fits remain statistically consistent within 2σ , and the derived indices are comparable to those seen in other radio-quiet systems (e.g., Coriat et al. 2011; Carotenuto et al. 2021b).

3.1 Distance ambiguity and the extreme nature of Swift J1727.8–1613

Regardless of the assumed distance, Swift J1727 exhibits an exceptionally radio-faint L_R – L_X evolution. Initially, Swift J1727 follows the steeper track seen in other radio-quiet sources (e.g., H1743–32), before diverging at lower X-ray luminosities and becoming markedly more radio-faint. Near the maximum plotted distance (~ 4 kpc), the source rejoins the standard track at $L_X \lesssim 10^{33} \text{ erg s}^{-1}$ ($L_R \sim 3 \times 10^{27} \text{ erg s}^{-1}$), \sim two orders of magnitude below typical rejoin values for radio-quiet systems. At this distance, Swift J1727's L_R – L_X behaviour mirrors that of MAXI J1348–630 and, potentially, MAXI J1631–472 if we adopt its minimum distance of 2 kpc (Monageng et al. 2021). At smaller distances—including the nominal estimate—Swift J1727 becomes the most radio-faint system in the L_R – L_X plane. For instance, at $D \sim 1.5$ kpc, rejoining occurs at $L_X \sim 10^{31} \text{ erg s}^{-1}$ ($L_R \sim 3 \times 10^{26} \text{ erg s}^{-1}$), nearly two orders of magnitude lower in X-rays than even MAXI J1348–630.

The low rejoining luminosity at the nearer distance estimates, together with the apparent consistency with MAXI J1348–630 at larger distances, could be interpreted as supporting a farther distance, i.e., $D > 4$ kpc. However, if the source lies beyond 4 kpc, its peak X-ray luminosity would be the highest reported for a hard state: $L_{X,\text{max}} \approx 5 \times 10^{38} (D/4.3 \text{ kpc})^2 \text{ erg s}^{-1}$, surpassing even the exceptionally bright GRS 1915+105 (Rushton et al. 2010), although Swift J1727 remains markedly fainter in the radio. Applying a bolometric correction factor of $\tau_{\text{bol}} \approx 2$ –5 (Migliari & Fender 2006; Anasopoulou et al. 2022) to convert from the 1–10 keV band to the total accretion luminosity, the peak hard state X-ray luminosity is consistent with a $\sim 7 M_\odot$ black hole exceeding its Eddington luminosity⁴: $L_{\text{edd}} = 1.26 \times 10^{38} (M_{\text{BH}}/M_\odot) \text{ erg s}^{-1}$.

The (bolometric) luminosity at which a state transition occurs is commonly expressed as a fraction of the Eddington luminosity, f_{edd} . Population studies of BH LMXB outbursts have found the hard→soft transitions most commonly occur at $f_{\text{edd}} \sim 0.1$ (Dunn et al. 2010; Tetarenko et al. 2016). This again suggests that an extreme hard-state luminosity, as implied by a large distance, may be disfavoured. Assuming a typical black hole mass, a closer distance would yield lower X-ray luminosities and a more typical f_{edd} . However, hard→soft transition luminosities span a broad distribution, and it is plausible for a system like Swift J1727 to reach Eddington-level luminosities prior to transitioning to the soft state (e.g., a lognormal distribution with $\mu \approx -0.9$, $\sigma \approx 0.4$; Tetarenko et al. 2016).

In contrast, the inverse soft→hard transition tends to occur more narrowly around $f_{\text{edd}} \sim 0.01$ – 0.04 (Maccarone 2003; Vahdat Motlagh et al. 2019). For Swift J1727, the X-ray luminosity at the time of this transition is $\approx 2 \times 10^{36} (D/2.6 \text{ kpc})^2 \text{ erg s}^{-1}$, implying $f_{\text{edd}} \approx 0.007 (D/2.6 \text{ kpc})^2$ (adopting $M_{\text{BH}} = 7 M_\odot$ and $\tau_{\text{bol}} = 3$). While the nominal distance yields an Eddington fraction consistent with population studies (e.g., the lognormal distribution with $\mu \approx -1.8$ and $\sigma \approx 0.3$ from Vahdat Motlagh et al. 2019), smaller distances quickly push the transition luminosity below the observed range for BH LMXBs. This discrepancy is more significant than that introduced by the aforementioned bright hard state, thereby favouring distances at or above the nominal estimate (though we note the existence of outliers with extremely low transitional luminosities, e.g., Tomsick et al. 2014; Chauhan et al. 2019).

In summary, while the distance to Swift J1727 remains uncertain, it is evident that across the range of distances, Swift J1727 stands out

as an exceptional system in terms of its L_R – L_X evolution and state transition behaviour.

3.2 Radio and X-ray spectral evolution

To our knowledge, Swift J1727 is also the radio-quiet system with the best-constrained X-ray spectral evolution during its L_R – L_X evolution. Like other BH LMXBs (both radio-quiet and radio-loud), the X-ray spectrum hardens to $\Gamma \sim 1.5$ – 1.6 during the initial decay, before softening as the source fades into quiescence (top two panels of Figure 2). Archival BH LMXBs exhibit a plateau at $\Gamma \sim 2.1$ as they approach and enter quiescence (e.g., Tomsick et al. 2001, 2004; Kong et al. 2002; Corbel et al. 2006; Plotkin et al. 2013; Reynolds et al. 2014). Given that our final epoch with spectral constraints yielded $\Gamma \sim 1.8$, we expect that Swift J1727 continued to soften after it became too faint for reliable spectral fitting. This places a lower limit of $\gtrsim 16$ days on the X-ray softening timescale (measured from the point of minimum Γ), consistent with other BH LMXBs. However, we note that the few systems with comparable constraints exhibit a broad range of softening timescales (3–90 days) (Tomsick et al. 2001; Kalemci et al. 2005; Armas Padilla et al. 2013; Plotkin et al. 2017a; Beri et al. 2019; Shaw et al. 2021). In contrast, a feature that appears unique to Swift J1727 is the apparent coincidence between the minimum Γ and the transition onto the shallow L_R – L_X track, suggesting a physical change in the accretion flow.

Accompanying the X-ray spectral evolution during the decay, the radio spectral index evolved from $\alpha \sim 0$ (self-absorbed) to ~ -0.7 (optically thin; bottom two panels of Figure 2). This change may reflect intrinsic variations in the compact jet (e.g., Corbel et al. 2013b; Plotkin et al. 2019; Russell et al. 2020). Alternatively, the compact jet may have faded, and we are now sampling residual (unsubtracted) ejecta emission. The latter scenario implies an even more radio-faint jet; however, our data do not allow us to distinguish between these possibilities.

4 DISCUSSION

We have presented the L_R – L_X evolution of Swift J1727 during its 2023–2024 outburst. Our coverage spans ~ 6.5 orders of magnitude in X-ray luminosity and ~ 4 in radio luminosity, revealing either an exceptionally X-ray bright rising hard state or the most radio-quiet decays observed, depending on the distance.

While the outlier track is considered standard L_R – L_X behaviour for radio-quiet sources, to date, there are only three (four with the inclusion of Swift J1727) BH LMXBs with monitoring that captured both the steep and shallow branches (H1743–32, Swift J1735.5–0127, and MAXI J1348–630; Coriat et al. 2011; Plotkin et al. 2017b; Carotenuto et al. 2021b). There is no consensus on the mechanisms that cause the radio-quiet and radio-loud evolutions, or whether they arise from differences in the properties of the jets or the accretion flows (or a combination of multiple factors). Here, we briefly discuss some of the explanations reported in the literature, considering their feasibility in light of the results presented here.

4.1 Jet-based origins

Several mechanisms have been proposed to explain the observed radio-quiet and radio-loud populations. Some attribute these differences to variations in the jet properties, which may be influenced by both intrinsic factors and observational biases. Espinasse & Fender

⁴ The Eddington luminosity is the luminosity at which radiation pressure overpowers gravity in the limit of a steady, spherical accretion of hydrogen.

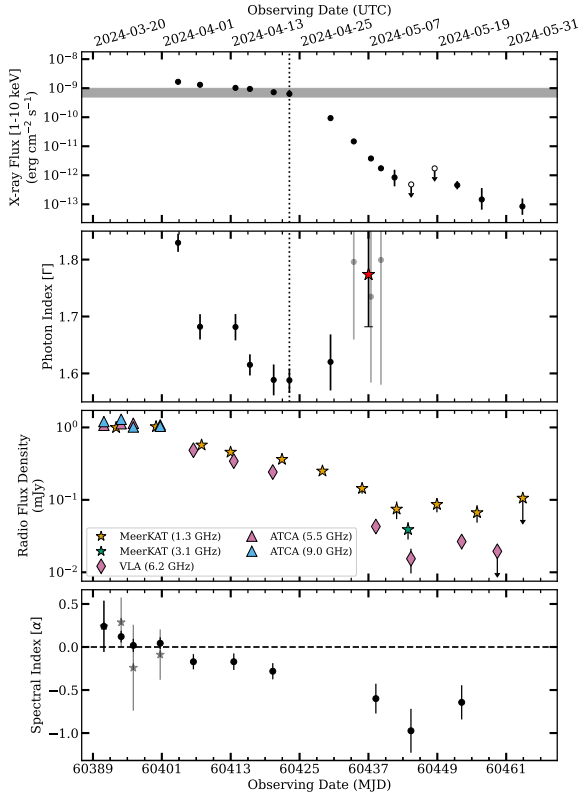


Figure 2. Spectral and photometric evolution of Swift J1727 during the decay hard state. X-ray flux in the 1–10 keV band (with the gray band highlighting the transitional flux range between the steep and shallow tracks; top panel), X-ray photon index Γ (with the red star indicating the variance-weighted average of the final three measurements; second panel), Radio flux density (with marker color indicating observing frequency and shape indicating facility; third panel), and radio spectral index α (with gray stars denoting ATCA-only measurements; bottom panel). The vertical dotted line in the top two panels marks the minimum Γ measurement. Notable spectral evolution includes the radio spectral index becoming optically thin as the flux density declines, and the photon index reaching a minimum just prior to the track transition.

(2018) investigated the correlation between a system’s radio spectral index and its classification as radio-loud or radio-quiet. The authors found statistically significant differences between the two populations: radio-quiet sources tended to have steeper spectral indices on average ($\alpha_{\text{avg}} \sim -0.3$) compared to the radio-loud population ($\alpha_{\text{avg}} \sim 0.2$). However, applying this result to Swift J1727 is not straightforward, as its spectral index varied significantly during its radio-quiet evolution ($-1 \lesssim \alpha \lesssim 0.3$).

Alternatively, Motta et al. (2018) proposed that the standard and hybrid L_R – L_X tracks could result from differences in viewing angle, rather than intrinsic differences between individual BH LMXBs. Their analysis revealed that radio-loud systems tend to have lower inclination angles than their radio-quiet counterparts, enhancing radio luminosity due to relativistic beaming. In the case of Swift J1727, modelling of its X-ray spectra (e.g., Peng et al. 2024; Svoboda et al. 2024; Liu et al. 2024) suggests a moderate inclination ~ 30 – 50° —comparable to estimates for most radio-loud sources (e.g. Motta et al. 2018). However, inclinations derived from X-ray spectral modelling are highly model-dependent. A more robust, albeit less constraining, upper limit of $< 74^\circ$ was inferred from the absence of optical variability due to gravitationally driven warping of the companion star (i.e., ellipsoidal modulation; Mata Sánchez et al. 2025).

In extreme systems, outbursts of low-inclination, highly beamed BH LMXBs have shown enhanced radio luminosities relative to the standard L_R – L_X track, particularly at higher X-ray luminosities. This deviation is typically attributed to an increasing jet speed—and thus increased beaming—with rising accretion rates (e.g., Russell et al. 2015; Zhang et al. 2025). However, even for distances corresponding to extreme X-ray luminosities, no radio enhancement was observed for Swift J1727; its rise hard state remains consistent with, or even below, the standard track. Assuming that relativistic beaming should affect the hard-state radio luminosities (i.e., its inclination is not near $\sim 70^\circ$), this could imply that Swift J1727’s compact jet is either intrinsically less relativistic than those of other low-to-moderate inclination systems, or that other factors more strongly modulate the observed radio emission (e.g. the stratified absorption scenario proposed by Motta et al. 2018). Given the totality of evidence, inclination alone does not appear to account for the radio-quiet nature of Swift J1727.

Magnetic fields are another property that could account for radio-quiet behaviour. Casella & Pe’er (2009) (and Pe’er & Casella 2009) proposed that strong internal magnetic fields within compact jets could suppress the observable radio emission. Unfortunately, we cannot assess the viability of this scenario from the L_R – L_X evolution alone. A more comprehensive investigation of the entire outburst—particularly the polarimetric evolution, which directly probes the magnetic field—may be essential to test this hypothesis. Strong magnetic fields remain a plausible explanation for the observed ‘radio-quietness’ of Swift J1727 and potentially other BH LMXBs.

4.2 Accretion-based origins

It is also possible that the apparent ‘radio-quietness’ arises not from a suppression of jet power, but rather from an enhancement in accretion luminosity. Radiatively efficient flows — such as luminous hot accretion flows (LHAFs; Yuan 2001) convert a larger fraction of the rest mass energy into radiation than radiatively inefficient flows, which predominantly advect energy across the event horizon or expel it via outflows (e.g., advection-dominated accretion flows, ADAFs; Narayan & Yi 1994). The radiative efficiency can be parameterised by η where $L_X = \eta \dot{M} c^2$, and \dot{M} is the mass accretion rate. In LHAFs, the radiative efficiency η can exceed that of ADAFs by an order of magnitude (Xie & Yuan 2012, 2016). These more efficient accretion flows have also been proposed to explain the distinct radio–X-ray correlations observed in AGN (Dong et al. 2014; Panessa et al. 2015). However, caution is warranted when comparing black hole LMXBs to AGN, as the latter—depending on their subclass—may exhibit significantly different accretion geometries and therefore may not serve as direct analogs to hard-state BH LMXBs (e.g., LHAFs versus thin disks).

Within this efficiency framework, there exists a critical mass accretion rate (\dot{M}_C) at which a system undergoes a transition to higher radiative efficiency (Narayan et al. 1998; Yuan 2001; Xie & Yuan 2012, 2016): $\dot{M}_C \approx 5\alpha_v^2 \theta_e^{3/2} \dot{M}_{\text{edd}}$, where $\alpha_v \sim 0.1$ – 1 (e.g., Tetarenko et al. 2018) characterizes the efficiency of angular momentum transport, $\theta_e \equiv k_B T_e / m_e c^2$ is the dimensionless electron temperature (e.g., $k_B T_e \sim 10$ – 1000 keV; Koljonen & Russell 2019; Yan et al. 2020), and $\dot{M}_{\text{edd}} = 10 L_{\text{edd}} / c^2$ is the Eddington mass accretion rate.

As $\dot{M} \rightarrow \dot{M}_C$, the radiative efficiency increases rapidly (e.g., $< 1\%$ to $\sim 8\%$; Xie & Yuan 2012). Once $\dot{M} > \dot{M}_C$, the flow becomes radiatively efficient, steepening the radio/X-ray correlation, $L_R \propto L_X^{-1.3}$ (see, Coriat et al. 2011, and references therein). In this picture, the shallow track represents an intermediate regime, where the system

transitions between the standard (radiatively inefficient) and steep (radiatively efficient) tracks. During this phase, L_X increases more rapidly than L_R for a given rise in \dot{M} (Xie & Yuan 2016). Systems with larger α_v or θ_e values exhibit higher critical accretion rate thresholds, \dot{M}_C , and may remain in a radiatively inefficient state for most—or even all—of an outburst, thereby appearing radio-loud. Recent broadband X-ray analyses have found evidence for a steeper L_R – L_X track at high X-ray luminosities ($\gtrsim 5 \times 10^{37} \text{ erg s}^{-1}$) in the canonical radio-loud source GX 339–4, supporting the interpretation that radio-loud evolutions can result from systems with significantly larger \dot{M}_C values (Islam & Zdziarski 2018; Koljonen & Russell 2019).

4.2.1 Did Swift J1727.8–1613 contain a radiatively efficient flow?

Intriguingly, the minimum observed Γ coincides with the inflection point in L_R – L_X where the correlation transitions from β_{steep} to β_{shallow} . For the first time in a radio-quiet system, we find evidence for the shallow L_R – L_X track coinciding with the onset of X-ray spectral softening. While such softening could arise from either inefficient accretion or jet-related processes (see, e.g. Corbel et al. 2006; Sobolewska et al. 2011; Plotkin et al. 2013), the alignment of the spectral transition and the ‘track switch’ strongly favours an accretion-driven origin. In particular, a jet-based explanation—such as the onset of synchrotron cooling at high energies—would predict a steeper correlation slope of $\beta > 1$ in L_R – L_X (Yuan & Cui 2005), contrary to what is observed. Thus, in Swift J1727, the X-ray softening appears consistent with the accretion flow evolution driving the shallow L_R – L_X track—possibly linked to the radiative efficiency transition discussed above.

Recognizing that the efficiency transition occurs during the shallow branch (i.e., when $L_X \lesssim L_{X,\text{tran}}$) we can use the relation $L_X = \eta \dot{M} c^2$ and the definition of \dot{M}_C , to derive the following expression:

$$M_{\text{BH}} \lesssim 10^{-4} \eta^{-1} \alpha_v^{-2} \theta_e^{-3/2} \left(\frac{D}{2.6 \text{ kpc}} \right)^2 M_{\odot}. \quad (2)$$

Although for Swift J1727, M_{BH} , α_v , θ_e , and D are not currently known—nor is any potential temporal evolution of these properties—-independent measurements of any subset of these parameters can help constrain the others. For example, adopting $\alpha_v \gtrsim 0.6$ and $kT_e \gtrsim 60 \text{ keV}$ at the lower-bound distance $D \approx 1.5 \text{ kpc}$ predicts $M_{\text{BH}} \lesssim 1 M_{\odot}$ (conservatively fixing $\eta = 0.01$), which is inconsistent with the lowest possible mass for a stellar-mass black hole. Multiwavelength constraints on key parameters—particularly distance—are likely essential for determining the nature of this system. More broadly, such constraints across a larger sample are crucial for understanding the physical origins behind the dramatic range of transitional luminosities (i.e. spanning more than six orders of magnitude; Islam & Zdziarski 2018; Koljonen & Russell 2019; Carotenuto et al. 2021b).

At all considered distances, the inferred (1–10 keV) transitional luminosity exceeds $5 \times 10^{35} \text{ erg s}^{-1}$, corresponding to $f_{\text{edd}} > 0.008$ (assuming $\tau_{\text{bol}} = 3$ and $M_{\text{BH}} = 7 M_{\odot}$). At these accretion rates, numerical simulations show that radiatively inefficient flows become unsustainable, indicating that Swift J1727 likely hosts a radiatively efficient accretion mode (at some point) during the outburst. However, this raises a deeper question: how do some systems remain on the standard (radio-loud) track well into the hard state, even at luminosities far exceeding this threshold (e.g., for $f_{\text{edd}} > 0.1$)? Indeed, current models struggle to reproduce the behavior of X-ray binaries in this regime (see Sądowski et al. 2017, and references therein).

It should be noted that our discussion is not intended as an exhaustive summary of the jet- or accretion-based mechanisms capable of producing the variation in L_R – L_X tracks, and the scenarios considered here—and those in the broader literature (e.g., Meyer-Hofmeister & Meyer 2014)—should not be viewed as mutually exclusive. Given the complexities of BH LMXBs, it is likely that multiple processes act in concert to enforce consistency with, or drive deviations from, the ‘standard’ L_R – L_X track, and their relative influence may vary throughout the outburst. While the precise mechanism(s) responsible for the behaviour of Swift J1727 remain uncertain, comprehensive datasets tracking anomalous behaviours such as this provide vital opportunities for testing our models and advancing our understanding of jet–accretion coupling.

5 CONCLUSION

We have presented the radio–X-ray evolution of the black hole low-mass X-ray binary Swift J1727.8–1613 during its 2023–2024 outburst. Our analysis, based on an extensive set of quasi-simultaneous radio and X-ray observations, allowed us to track the jet–accretion coupling over ~ 6.5 orders of magnitude in X-ray luminosity and ~ 4 in radio luminosity.

- The source exhibited a broken power-law evolution with well-constrained steep and shallow branches, characteristic of a hybrid (radio-quiet) track.
- For the first time in a radio-quiet system, we found the transition to the shallow track coincided with the onset of X-ray spectral softening, suggesting a link to changes in the accretion flow.
- The radio–X-ray track of Swift J1727.8–1613 is highly sensitive to the assumed distance. At $D \sim 1.5$ – 4.0 kpc , the source rejoins the standard track at extremely low luminosities ($L_X \sim 10^{31}$ – $10^{32} \text{ erg s}^{-1}$), making it the most radio-quiet (BH LMXB) evolution identified to date. However, at the upper end of the credible distance range ($D \gtrsim 4.0 \text{ kpc}$), its radio luminosity becomes broadly consistent with sources like MAXI J1348–630, placing Swift J1727 near the faint edge of the archival radio-quiet population.
- If Swift J1727.8–1613 lies near the upper end of the considered distance range ($D \gtrsim 4 \text{ kpc}$), its peak 1–10 keV X-ray luminosity reaches $L_X \gtrsim 5 \times 10^{38} \text{ erg s}^{-1}$. Applying a typical bolometric correction factor ($\tau_{\text{bol}} \sim 2$ – 5), this implies a bolometric luminosity exceeding the Eddington luminosity of a $\sim 7 M_{\odot}$ black hole. In this scenario, Swift J1727 would represent the most X-ray luminous hard-state BH LMXB observed to date in the L_R – L_X plane.

While multiple jet- and accretion-based mechanisms have been proposed to explain radio-quiet behaviour, it remains unclear which (or what combination of) mechanisms can fully account for Swift J1727’s properties. The coincidence of X-ray softening with the transition to the shallow L_R – L_X track favours, in part, an accretion-driven evolution—possibly tied to a change in radiative efficiency—over purely jet-based explanations. Future constraints on the distance, multiwavelength spectral modelling, and polarimetric monitoring will be key to clarifying the physical drivers behind the diversity in jet–accretion coupling observed across BH LMXBs.

ACKNOWLEDGEMENTS

AKH thanks UKRI for support. AJT acknowledges that this research was undertaken thanks to funding from the Canada Research Chairs Program and the support of the Natural Sciences and Engineering

Research Council of Canada (NSERC; funding reference number RGPIN-2024-04458). FC acknowledges support from the Royal Society through the Newton International Fellowship programme (NIF/R1/211296). TDR is an INAF IAF fellow. RS acknowledges the INAF grant number 1.05.23.04.04. JvdE acknowledges a Warwick Astrophysics prize post-doctoral fellowship made possible thanks to a generous philanthropic donation, and was supported by funding from the European Union's Horizon Europe research and innovation programme under the Marie Skłodowska-Curie grant agreement No 101148693 (MeerSHOCKS) for part of this work. CMW acknowledges financial support from the Forrest Research Foundation Scholarship, the Jean-Pierre Macquart Scholarship, and the Australian Government Research Training Program Scholarship. This project has received funding from the European Research Council (ERC) under the European Union's Horizon 2020 research and innovation programme (grant agreement No. 101002352, PI: M. Linares). RF thanks UKRI, The ERC and The Hintze Family Charitable Foundation for support. RMP acknowledges support from NASA under award No. 80NSSC23M0104. DMR and PS are supported by Tamkeen under the NYU Abu Dhabi Research Institute grant CASS.

The National Radio Astronomy Observatory is a facility of the National Science Foundation operated under cooperative agreement by Associated Universities, Inc. The MeerKAT telescope is operated by the South African Radio Astronomy Observatory, which is a facility of the National Research Foundation, an agency of the Department of Science and Innovation. We acknowledge the use of the Inter-University Institute for Data Intensive Astronomy (IDIA) data intensive research cloud for data processing. IDIA is a South African university partnership involving the University of Cape Town, the University of Pretoria and the University of the Western Cape. The Australia Telescope Compact Array is part of the Australia Telescope National Facility which is funded by the Australian Government for operation as a National Facility managed by CSIRO. We acknowledge the Gomeri people as the traditional owners of the ATCA observatory site.

DATA AVAILABILITY

Data from the VLA are available through the VLA data archive (Project IDs: 23A–260, 2B–069, and 3B–064): <https://data.nrao.edu/portal/>. Data from MeerKAT are available through the SRAO data archive (Proposal IDs: SCI-20180516-PW-01 and SCI-20230907-RF-01): <https://archive.srao.ac.za/>. Data from ATCA are available through the ATNF archive (Project codes: C2601, C3057, and C3362): <https://atoa.atnf.csiro.au>. Data from the *Swift*-XRT are publicly available through the *Swift* archive: https://www.swift.ac.uk/swift_portal. We host machine-readable data files and analysis scripts at https://github.com/AKHughes1994/SwJ1727_2023_Outburst.

REFERENCES

- Alabarta K., et al., 2021, *MNRAS*, **507**, 5507
- Anastasopoulou K., Zezas A., Steiner J. F., Reig P., 2022, *MNRAS*, **513**, 1400
- Armas Padilla M., Degenaar N., Russell D. M., Wijnands R., 2013, *MNRAS*, **428**, 3083
- Araud K. A., 1996, in Jacoby G. H., Barnes J., eds, *Astronomical Society of the Pacific Conference Series Vol. 101, Astronomical Data Analysis Software and Systems V*. p. 17
- Bahramian A., Rushton A., 2022, bersavosh/XRB-LrLx_pub: update 20220908, doi:10.5281/zenodo.7059313, <https://doi.org/10.5281/zenodo.7059313>
- Belloni T. M., Motta S. E., 2016, in Bambi C., ed., *Astrophysics and Space Science Library Vol. 440, Astrophysics of Black Holes: From Fundamental Aspects to Latest Developments*. p. 61 (arXiv:1603.07872), doi:10.1007/978-3-662-52859-4_2
- Beri A., et al., 2019, *MNRAS*, **485**, 3064
- Bollemeijer N., et al., 2023a, *The Astronomer's Telegram*, **16247**, 1
- Bollemeijer N., et al., 2023b, *The Astronomer's Telegram*, **16273**, 1
- Bright J. S., et al., 2020, *Nature Astron.*, **4**, 697
- Brocksopp C., Jonker P. G., Fender R. P., Groot P. J., van der Klis M., Tingay S. J., 2001, *MNRAS*, **323**, 517
- Brocksopp C., et al., 2002, *MNRAS*, **331**, 765
- Burridge B. J., et al., 2025, arXiv e-prints, p. arXiv:2502.06448
- Burrows D. N., et al., 2005, *Space Sci. Rev.*, **120**, 165
- Carotenuto F., et al., 2021a, *MNRAS*, **504**, 444
- Carotenuto F., et al., 2021b, *Monthly Notices of the Royal Astronomical Society: Letters*, **505**, L58
- Carotenuto F., Corbel S., Tzioumis A., 2022, *MNRAS*, **517**, L21
- Casella P., Pe'er A., 2009, *ApJ*, **703**, L63
- Cash W., 1979, *ApJ*, **228**, 939
- Chauhan J., et al., 2019, *MNRAS*, **488**, L129
- Corbel S., Nowak M. A., Fender R. P., Tzioumis A. K., Markoff S., 2003, *A&A*, **400**, 1007
- Corbel S., Tomsick J. A., Kaaret P., 2006, *ApJ*, **636**, 971
- Corbel S., Coriat M., Brocksopp C., Tzioumis A. K., Fender R. P., Tomsick J. A., Buxton M. M., Bailyn C. D., 2013a, *MNRAS*, **428**, 2500
- Corbel S., et al., 2013b, *MNRAS*, **431**, L107
- Coriat M., et al., 2011, *MNRAS*, **414**, 677
- Corral-Santana J. M., Casares J., Muñoz-Darias T., Bauer F. E., Martínez-Pais I. G., Russell D. M., 2016, *A&A*, **587**, A61
- De Marco B., Motta S. E., Belloni T. M., 2022, in Bambi C., Sanganello A., eds., *Handbook of X-ray and Gamma-ray Astrophysics*. p. 58, doi:10.1007/978-981-16-4544-0_129-1
- Done C., Gierliński M., Kubota A., 2007, *A&ARv*, **15**, 1
- Dong A.-J., Wu Q., Cao X.-F., 2014, *ApJ*, **787**, L20
- Drachis P. A., et al., 2023, *The Astronomer's Telegram*, **16219**, 1
- Dunn R. J. H., Fender R. P., Körding E. G., Belloni T., Cabanac C., 2010, *MNRAS*, **403**, 61
- Espinasse M., Fender R., 2018, *MNRAS*, **473**, 4122
- Evans P. A., et al., 2007, *A&A*, **469**, 379
- Evans P. A., et al., 2009, *MNRAS*, **397**, 1177
- Fender R., 2006, in , Vol. 39, *Compact stellar X-ray sources*. pp 381–419, doi:10.48550/arXiv.astro-ph/0303339
- Fender R. P., Garrington S. T., McKay D. J., Muxlow T. W. B., Pooley G. G., Spencer R. E., Stirling A. M., Waltman E. B., 1999a, *MNRAS*, **304**, 865
- Fender R., et al., 1999b, *ApJ*, **519**, L165
- Fender R. P., Belloni T. M., Gallo E., 2004, *MNRAS*, **355**, 1105
- Gallo E., Fender R. P., Pooley G. G., 2003, *MNRAS*, **344**, 60
- Gallo E., Corbel S., Fender R. P., Maccarone T. J., Tzioumis A. K., 2004, *MNRAS*, **347**, L52
- Gallo E., et al., 2014, *MNRAS*, **445**, 290
- Gallo E., Degenaar N., van den Eijnden J., 2018, *MNRAS*, **478**, L132
- Hannikainen D. C., Hunstead R. W., Campbell-Wilson D., Sood R. K., 1998, *A&A*, **337**, 460
- Heywood I., et al., 2016, *MNRAS*, **460**, 4433
- Ingram A., et al., 2023, arXiv e-prints, p. arXiv:2311.05497
- Islam N., Zdziarski A. A., 2018, *MNRAS*, **481**, 4513
- Jonker P. G., et al., 2010, *MNRAS*, **401**, 1255
- Kalemci E., Tomsick J. A., Buxton M. M., Rothschild R. E., Pottschmidt K., Corbel S., Brocksopp C., Kaaret P., 2005, *ApJ*, **622**, 508
- Kalemci E., Kara E., Tomsick J. A., 2022, in Bambi C., Sanganello A., eds., *Handbook of X-ray and Gamma-ray Astrophysics*. p. 9, doi:10.1007/978-981-16-4544-0_100-1
- Kennea J. A., Swift Team 2023, *GRB Coordinates Network*, **34540**, 1
- Koljonen K. I. I., Russell D. M., 2019, *ApJ*, **871**, 26

- Kong A. K. H., McClintock J. E., Garcia M. R., Murray S. S., Barret D., 2002, *ApJ*, **570**, 277
- Liu H.-X., et al., 2024, *arXiv e-prints*, p. [arXiv:2406.03834](#)
- Livio M., 2002, *Nature*, **417**, 125
- Maccarone T. J., 2003, *A&A*, **409**, 697
- Maccarone T. J., Osler A., Miller-Jones J. C. A., Atri P., Russell D. M., Meier D. L., McHardy I. M., Longa-Peña P. A., 2020, *MNRAS*, **498**, L40
- Massardi M., Bonaldi A., Bonavera L., López-Caniego M., de Zotti G., Ekers R. D., 2011, *MNRAS*, **415**, 1597
- Mata Sánchez D., Muñoz-Darias T., Armas Padilla M., Casares J., Torres M. A. P., 2024, *A&A*, **682**, L1
- Mata Sánchez D., Torres M. A. P., Casares J., Muñoz-Darias T., Armas Padilla M., Yanes-Rizo I. V., 2025, *A&A*, **693**, A129
- Matsuoka M., et al., 2009, *PASJ*, **61**, 999
- McClintock J. E., Remillard R. A., 2006, *Black hole binaries*. Cambridge University Press, pp 157–213
- McConnell D., Sadler E. M., Murphy T., Ekers R. D., 2012, *MNRAS*, **422**, 1527
- Merloni A., Heinz S., di Matteo T., 2003, *MNRAS*, **345**, 1057
- Meyer-Hofmeister E., Meyer F., 2014, *A&A*, **562**, A142
- Migliari S., Fender R. P., 2006, *MNRAS*, **366**, 79
- Mihara T., et al., 2011, *PASJ*, **63**, S623
- Miller-Jones J. C. A., Sivakoff G. R., Bahramian A., Russell T. D., 2023a, *The Astronomer's Telegram*, **16211**, 1
- Miller-Jones J. C. A., Bahramian A., Altamirano D., Homan J., Russell T. D., Sivakoff G. R., 2023b, *The Astronomer's Telegram*, **16271**, 1
- Mirabel I. F., Rodríguez L. F., 1994, *Nature*, **371**, 46
- Monageng I. M., Motta S. E., Fender R., Yu W., Woudt P. A., Tremou E., Miller-Jones J. C. A., van der Horst A. J., 2021, *MNRAS*, **501**, 5776
- Motta S. E., Casella P., Fender R. P., 2018, *MNRAS*, **478**, 5159
- Narayan R., Yi I., 1994, *ApJ*, **428**, L13
- Narayan R., Mahadevan R., Quataert E., 1998, in Abramowicz M. A., Björnsson G., Pringle J. E., eds, *Theory of Black Hole Accretion Disks*. pp 148–182 ([arXiv:astro-ph/9803141](#)), doi:10.48550/arXiv.astro-ph/9803141
- O'Connor B., Hare J., Younes G., Gendreau K., Arzoumanian Z., Ferrara E., 2023, *The Astronomer's Telegram*, **16207**, 1
- Page K. L., Dichiara S., Gropp J. D., Krimm H. A., Parsotan T. M., Williams M. A., Neil Gehrels Swift Observatory Team 2023, *GRB Coordinates Network*, **34537**, 1
- Panessa F., et al., 2015, *MNRAS*, **447**, 1289
- Pe'er A., Casella P., 2009, *ApJ*, **699**, 1919
- Peng J.-Q., et al., 2024, *ApJ*, **960**, L17
- Plotkin R. M., Gallo E., Jonker P. G., 2013, *ApJ*, **773**, 59
- Plotkin R. M., et al., 2017a, *ApJ*, **834**, 104
- Plotkin R. M., et al., 2017b, *ApJ*, **848**, 92
- Plotkin R. M., Miller-Jones J. C. A., Chomiuk L., Strader J., Bruzewski S., Bundas A., Smith K. R., Ruan J. J., 2019, *ApJ*, **874**, 13
- Podgorny J., Svoboda J., Dovciak M., 2024, *The Astronomer's Telegram*, **16541**, 1
- Reynolds M. T., Reis R. C., Miller J. M., Cackett E. M., Degenaar N., 2014, *MNRAS*, **441**, 3656
- Rushton A., Spencer R., Fender R., Pooley G., 2010, *A&A*, **524**, A29
- Russell D. M., Miller-Jones J. C. A., Maccarone T. J., Yang Y. J., Fender R. P., Lewis F., 2011, *ApJ*, **739**, L19
- Russell T. D., et al., 2015, *MNRAS*, **450**, 1745
- Russell T. D., et al., 2019a, *ApJ*, **883**, 198
- Russell T. D., et al., 2019b, *ApJ*, **883**, 198
- Russell T. D., et al., 2020, *MNRAS*, **498**, 5772
- Russell T. D., Carotenuto F., Miller-Jones J. C. A., Atri P., Grollmund N., Corbel S., et al. 2024, *The Astronomer's Telegram*, **16552**, 1
- Shapiro S. L., Lightman A. P., Eardley D. M., 1976, *ApJ*, **204**, 187
- Shaw A. W., et al., 2021, *ApJ*, **907**, 34
- Sądowski A., Wielgus M., Narayan R., Abarca D., McKinney J. C., Chael A., 2017, *MNRAS*, **466**, 705
- Sobolewska M. A., Papadakis I. E., Done C., Malzac J., 2011, *MNRAS*, **417**, 280
- Stiele H., Kong A. K. H., 2024, *A&A*, **691**, A268
- Svoboda J., et al., 2024, *arXiv e-prints*, p. [arXiv:2403.04689](#)
- Tananbaum H., Gursky H., Kellogg E. M., Levinson R., Schreier E., Giacconi R., 1972, *ApJ*, **174**, L143
- Tetarenko B. E., Sivakoff G. R., Heinke C. O., Gladstone J. C., 2016, *ApJS*, **222**, 15
- Tetarenko B. E., Lasota J. P., Heinke C. O., Dubus G., Sivakoff G. R., 2018, *Nature*, **554**, 69
- Thorne K. S., Price R. H., 1975, *ApJ*, **195**, L101
- Tomsick J. A., Corbel S., Kaaret P., 2001, *ApJ*, **563**, 229
- Tomsick J. A., Kalemci E., Kaaret P., 2004, *ApJ*, **601**, 439
- Tomsick J. A., Yamaoka K., Corbel S., Kalemci E., Migliari S., Kaaret P., 2014, *ApJ*, **791**, 70
- Vahdat Motlagh A., Kalemci E., Maccarone T. J., 2019, *MNRAS*, **485**, 2744
- Williams D. R. A., et al., 2020, *MNRAS*, **491**, L29
- Wilms J., Allen A., McCray R., 2000, *ApJ*, **542**, 914
- Wood C. M., et al., 2021, *MNRAS*, **505**, 3393
- Wood C. M., et al., 2024, *arXiv e-prints*, p. [arXiv:2405.12370](#)
- Wood C. M., et al., 2025, *arXiv e-prints*, p. [arXiv:2503.03073](#)
- Xie F.-G., Yuan F., 2012, *MNRAS*, **427**, 1580
- Xie F.-G., Yuan F., 2016, *MNRAS*, **456**, 4377
- Yan Z., Xie F.-G., Zhang W., 2020, *ApJ*, **889**, L18
- Yu W., 2023, *The Astronomer's Telegram*, **16276**, 1
- Yuan F., 2001, *MNRAS*, **324**, 119
- Yuan F., Cui W., 2005, *ApJ*, **629**, 408
- Zhang X., et al., 2025, *MNRAS*, **538**, L43

¹*Department of Physics, University of Oxford, Denys Wilkinson Building, Keble Road, Oxford OX1 3RH, UK*

²*INAF-Osservatorio Astronomico di Roma, Via Frascati 33, I-00078, Monte Porzio Catone (RM), Italy*

³*INAF, Istituto di Astrofisica Spaziale e Fisica Cosmica, Via U. La Malfa 153, I-90146 Palermo, Italy*

⁴*Department of Physics and Astronomy, University of Lethbridge, Lethbridge, Alberta, T1K 3M4, Canada*

⁵*International Centre for Radio Astronomy Research, Curtin University, GPO Box U1987, Perth, WA 6845, Australia*

⁶*Department of Physics, University of Nevada, Reno, NV 89557, USA*

⁷*Nevada Center for Astrophysics, University of Nevada, Las Vegas, NV 89154, USA*

⁸*Breakthrough Listen, Astrophysics, Department of Physics, The University of Oxford, Keble Road, Oxford, OX1 3RH, UK*

⁹*Department of Astronomy, University of Cape Town, Private Bag X3, Rondebosch 7701, South Africa*

¹⁰*Department of Physics and Astronomy, The University of Sheffield, Hicks Building, Hounsfield Road, Sheffield S3 7RH, UK*

¹¹*Center for Astrophysics | Harvard & Smithsonian, 60 Garden Street, Cambridge, MA, 02138*

¹²*Department of Physics, University of Alberta, CCIS 4-181, Edmonton, AB T6G 2E1*

¹³*Jodrell Bank Centre for Astrophysics, School of Physics and Astronomy, The University of Manchester, Manchester, M13 9PL, UK*

¹⁴*School of Physics & Astronomy, University of Southampton, SO17 1BJ, UK*

¹⁵*Department of Physics, University of Warwick, Gibbet Hill Road, Coventry, CV4 7AL, UK*

¹⁶*Université Paris Cité and Université Paris Saclay, CEA, CNRS, AIM, F-91190 Gif-sur-Yvette, France*

¹⁷*Department of Astrophysical and Planetary Sciences, JILA, Duane Physics Bldg., 2000 Colorado Ave., University of Colorado, Boulder, CO 80309, USA*

¹⁸*Anton Pannekoek Institute for Astronomy, Universiteit van Amsterdam, Science Park 904, 1098, XH, Amsterdam, The Netherlands*

¹⁹*Department of Astronomy, University of Michigan, 1085 S University, Ann Arbor, MI 48109, USA*

²⁰*Department of Physics, Norwegian University of Science and Technology, NO-7491 Trondheim, Norway*

²¹*Department of Physics and Astronomy, Texas Tech University, Lubbock, TX 79409-1051, USA*

²²*Gravitation and Astroparticle Physics Amsterdam Institute, University of Amsterdam, Science Park 904, 1098 XH 195 196 Amsterdam, The Netherlands*

²³*Istituto Nazionale di Astrofisica, Osservatorio Astronomico di Brera, Via E. Bianchi 46, 23807 Merate, (LC), Italy*

²⁴*Center for Astrophysics and Space Science (CASS), New York University Abu Dhabi, PO Box 129188, Abu Dhabi, UAE*

²⁵*Department of Physics and Astronomy, Butler University, 4600 Sunset Avenue, Indianapolis, IN 46208, USA*

²⁶*INAF-Osservatorio Astrofisico di Torino, Strada Osservatorio 20, I-10025 Pino Torinese, Italy*

²⁷*Sydney Institute for Astronomy, School of Physics A28, The University of Sydney, Sydney, NSW 2006, Australia*

²⁸*Space Sciences Lab, University of California, Berkeley, 7 Gauss Way, Berkeley, CA 94720, USA*

²⁹*Shanghai Astronomical Observatory, Chinese Academy of Sciences, Shanghai 200030, China*

³⁰*University of Chinese Academy of Sciences, Chinese Academy of Sciences, Beijing 100049, China*

APPENDIX A: LIGHT CURVES AND INTERPOLATION

Figure A1 presents a multi-wavelength photometric and spectral view of the 2023–2024 outburst of Swift J1727. From top to bottom: (i) the 2–20 keV flux from the Monitor of All sky X-ray Image Gas Slit Camera (MAXI/GSC, *top panel*; Matsuoka et al. 2009; Mihara et al. 2011); (ii) the X-ray hardness ratio, defined as the ratio of flux from the 2–6 keV and 6–20 keV MAXI/GSC fluxes (*second panel*); (iii) the Meerkat, VLA, and ATCA light curves originally presented in Hughes et al. (Submitted); and (iv) the inter-band radio spectral indices from simultaneous multi-frequency VLA and ATCA observations (*bottom panel*).

Shaded grey indicates the rise and decay hard states. The vertical dot-dashed and dashed lines mark the reported hard→soft and soft→hard transitions, respectively (Bollemeijer et al. 2023a,b; Podgorny et al. 2024; Russell et al. 2024). As discussed in the main text, we truncate the rise hard state earlier than the reported transition to avoid contamination from flaring activity that launches multiple jet ejecta (Wood et al. 2025). These ejections, unresolved at the angular resolution of our instruments 60190.166, would be spatially coincident with the compact jet. Their presence is reflected in the radio spectral index evolution (*bottom panel*), which displays significant variability between the rise hard state grey region and the reported transition, indicative of a rapidly evolving population of jet components.

The radio light curves shown in Hughes et al. (Submitted) represent the total integrated flux densities. Consequently, for epochs with multiple spatial components (e.g., the compact jet and discrete ejecta), the fluxes in Figure A1 reflect the sum of multiple components. While the (included) rising hard state only includes compact jet emission, the decay hard state features bright, resolved southern-moving ejecta (Figure A2), which become the dominant radio source at late times. This leads to the plateau seen in the radio decay phase of Figure A1. For a clearer view of the compact core evolution, we present core-only light curves in Figures A3 and A4. Furthermore, we show both the measured and interpolated X-ray flux values, con-

firmed that our linear interpolation method neither introduces nor smooths over real X-ray variability.

APPENDIX B: EXPONENTIAL FIT AND DECAY SUBTRACTION

The image morphology (Figure A2) and radio light curves (Figure A4) indicate the presence of core emission during the soft state. Since compact jets are expected to be quenched in this state, and the observed core emission is spectrally steep ($\alpha \sim -1$, third panel of Figure A1), we interpret the soft state core emission as arising from unresolved jet ejecta. After compact jet reformation, the core emission becomes a superposition of components. However, only the compact jet contribution is relevant for the L_R – L_X plane.

To isolate the compact jet emission, we modelled the fading ejecta as an exponential decay,

$$F_{R,\nu_0} = Ae^{-\frac{t}{\tau}}, \quad (\text{B1})$$

where $\nu_0 = 1.28$ GHz corresponds to the MeerKAT observing frequency. We fit this model using the final five MeerKAT epochs and subtracted the resulting flux from each observation to estimate the compact jet contribution. We find a decay timescale of $\tau = 20.5 \pm 0.8$ days, similar to previous measurements of BH LMXB ejecta decays (e.g. $\tau = 21.0 \pm 0.9$ days; see extended data Fig.3 of Bright et al. 2020). Because our radio observations span a wide range of frequencies ($\nu \sim 1$ –10 GHz), we scaled the model flux to the appropriate observing frequency using a power law spectrum: $F_{R,\nu} = F_{R,\nu_0}(\nu/\nu_0)^{\alpha_{ej}}$. We adopt $\alpha_{ej} = -1$, consistent with the inter-band ATCA spectral indices measured at the end of the soft state (third panel of Fig. A1).

Figure B1 displays the exponential fit and the resulting residuals interpreted as compact jet emission. We address the potential for incomplete subtraction and its implications in the main text.

APPENDIX C: DATA TABLE

Table C1 summarises the final radio and X-ray measurements presented in Figure 1, assuming a distance of $D=2.6$ kpc. The X-ray luminosities are interpolated to match the epochs of the radio observations. The table also includes the corresponding spectral indices and observing frequencies used to scale the radio luminosities to 5 GHz.

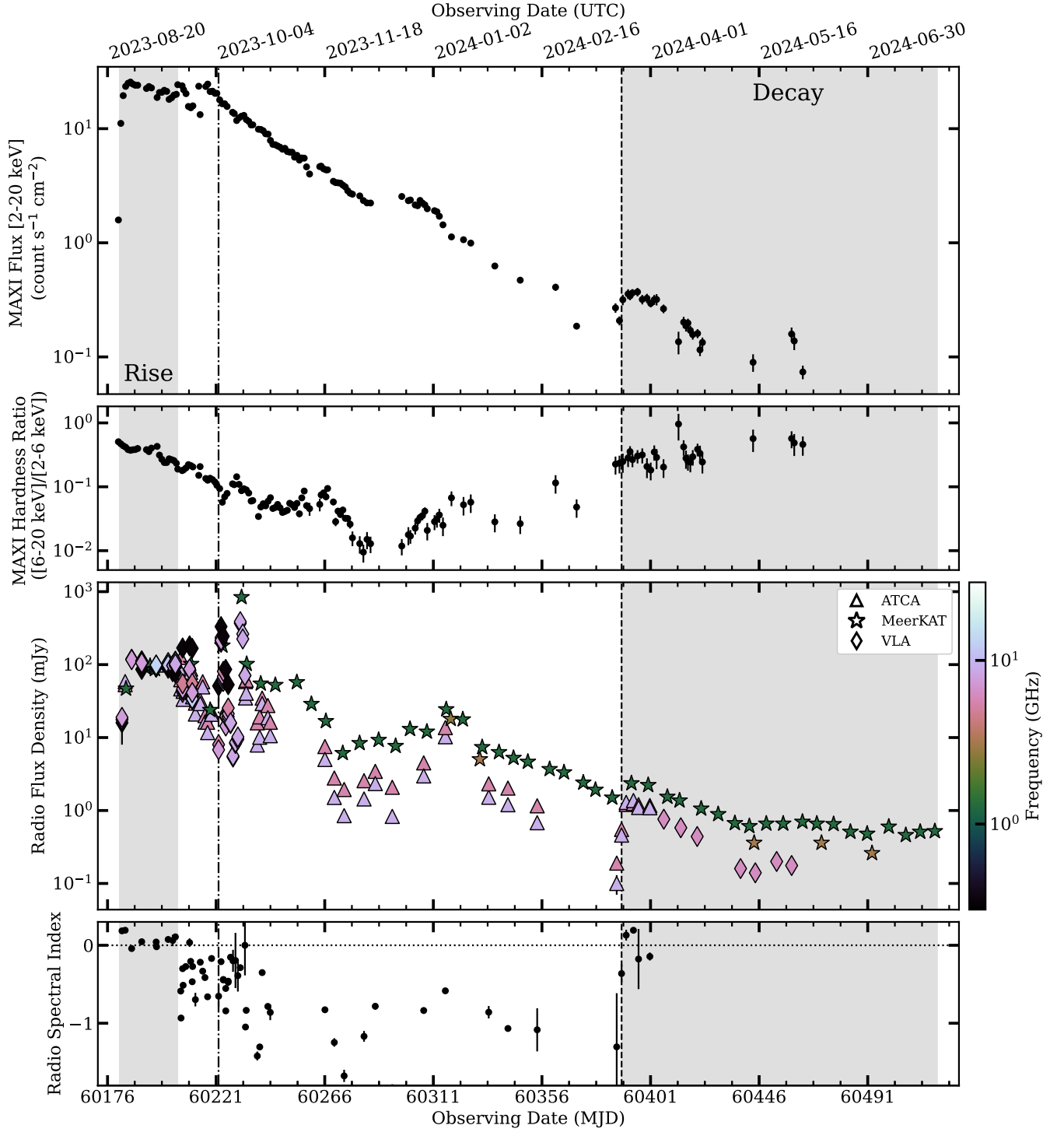


Figure A1. Radio and X-ray light curves covering the entirety of the 2023–2024 outburst of Swift J1727: MAXI/GSC 2–20 keV X-ray flux (*top panel*); X-ray hardness ratio calculated from the 2–6 keV and 6–20 keV sub-bands (*second panel*); MeerKAT, VLA, and ATCA light (multi-frequency) light curves (*third panel*); inter-band radio spectral indices (*bottom panel*). The dashed-dotted and dashed lines correspond to the hard→soft and soft→hard transitions reported in the literature (Bollemeijer et al. 2023a,b; Podgorny et al. 2024; Russell et al. 2024). The grey shaded regions highlight the times used for the rising and decaying hard states presented in this work. We truncated the rise hard state before the reported state transition due to the onset of flaring and transient jet ejections (Wood et al. 2025).

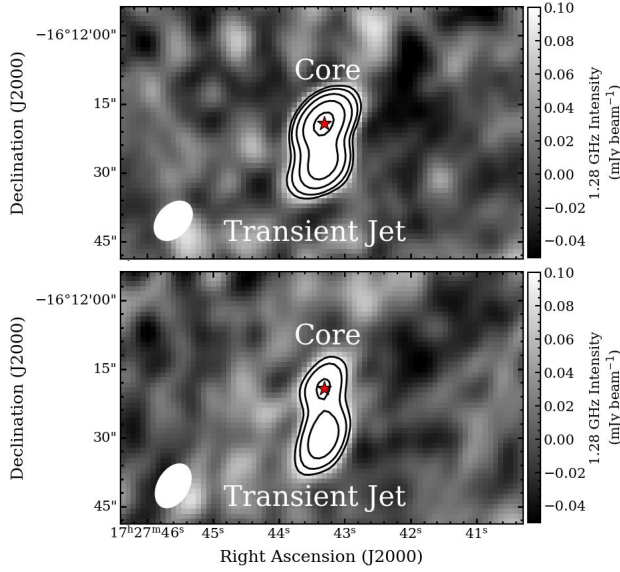


Figure A2. Sample radio images of Swift J1727 from: 2024 March 4 (MJD 60373) while the source was in the soft state (*top panel*); and 2024 April 28 (MJD 60428) after the soft→hard transition (i.e., the decay hard state, *bottom panel*). The red star indicates the radio position of the core, as measured by the VLA and reported in Miller-Jones et al. (2023a). Even while Swift J1727 was in the soft state, during which compact jet emission is quenched, there is still bright core emission from unresolved jet ejecta. Additionally, there is a resolved transient jet south of the core position. This resolved jet dominates the integrated flux density at the end of the outburst.

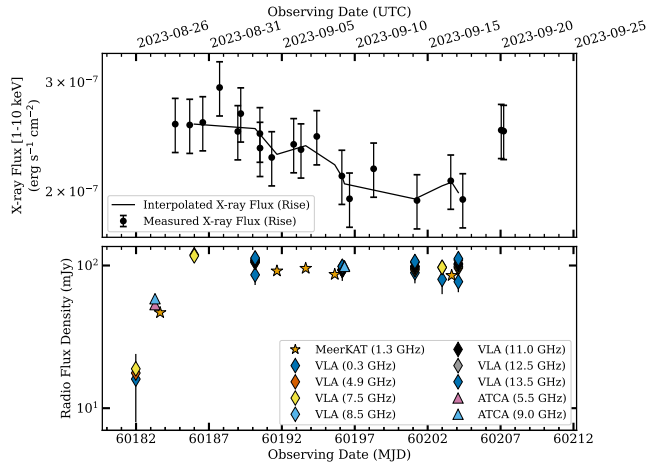


Figure A3. Light curves showing the (*Swift*-XRT) 1–10 keV X-ray flux (*top panel*) and core radio flux densities (*bottom panel*) during the rise hard state of Swift J1727. Solid lines in the top panel trace X-ray fluxes interpolated onto the radio observation epochs (with data points marked by vertices), while black circles indicate the (unabsorbed) X-ray fluxes as measured by *Swift*-XRT. Interpolation was performed in log-space. For clarity, error bars on the interpolated X-ray fluxes are omitted, but those on the measurements are representative of the adopted uncertainties.

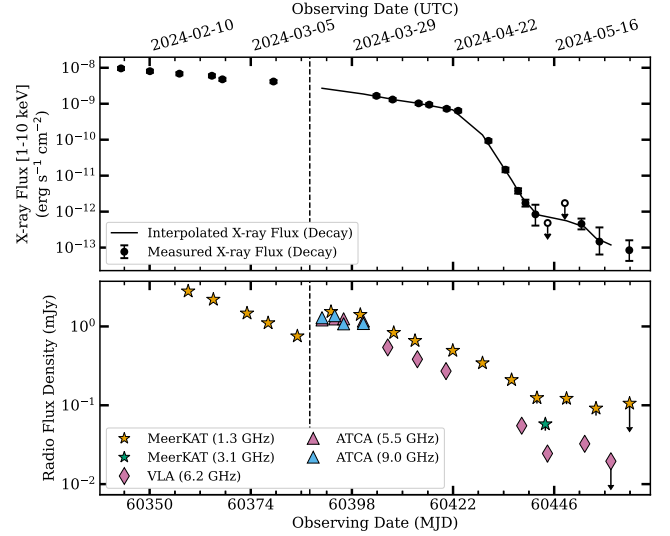


Figure A4. Same as Figure A3 but for the decay hard state. The vertical dashed line marks the soft→hard state transition (Podgorny et al. 2024; Russell et al. 2024).

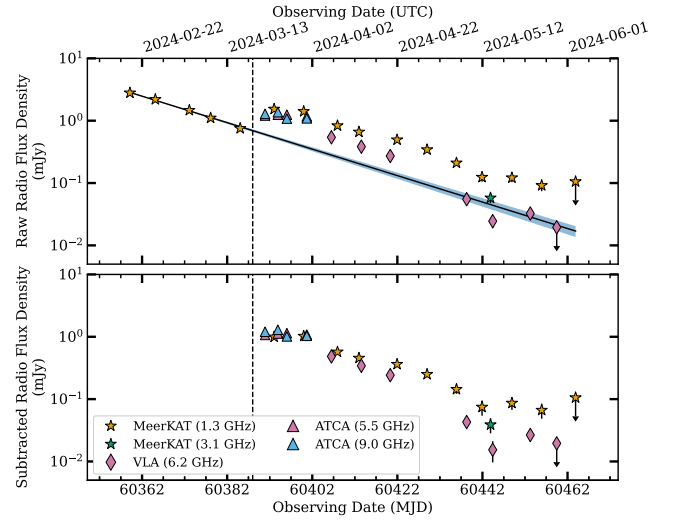


Figure B1. The decaying hard state: measured radio flux densities (*top panel*); radio flux densities after subtraction of the exponentially decaying soft state component (*bottom panel*). The solid black line and shaded blue area correspond to the exponential fit (to the 1.28 GHz observations) and the 68% confidence interval, respectively. The vertical dashed line marks the soft→hard state transition (Podgorny et al. 2024; Russell et al. 2024).

This paper has been typeset from a \LaTeX file prepared by the author.

Date (UTC)	Date (MJD)	L_X [1–10 keV] (erg s $^{-1}$)	L_R [5 GHz] (erg s $^{-1}$)	α	ν_{obs} (GHz)
2023-08-29T23:49:29	60185.993	$(2.08^{+0.15}_{-0.16}) \times 10^{38}$	$(4.8 \pm 0.5) \times 10^{30}$	-0.042 ± 0.001	5.20
2023-09-03T03:59:36	60190.166	$(2.05^{+0.16}_{-0.17}) \times 10^{38}$	$(4.3 \pm 0.4) \times 10^{30}$	$+0.046 \pm 0.001$	4.75
2023-09-04T15:55:43	60191.664	$(1.86^{+0.15}_{-0.15}) \times 10^{38}$	$(3.9 \pm 0.4) \times 10^{30}$	$+0.046 \pm 0.001$	1.28
2023-09-06T15:14:06	60193.635	$(1.92^{+0.15}_{-0.15}) \times 10^{38}$	$(4.1 \pm 0.4) \times 10^{30}$	$+0.042 \pm 0.001$	1.28
2023-09-08T15:05:28	60195.629	$(1.79^{+0.14}_{-0.14}) \times 10^{38}$	$(3.7 \pm 0.4) \times 10^{30}$	$+0.042 \pm 0.001$	1.28
2023-09-09T03:29:39	60196.146	$(1.71^{+0.16}_{-0.16}) \times 10^{38}$	$(3.8 \pm 0.4) \times 10^{30}$	$+0.042 \pm 0.001$	4.75
2023-09-09T07:06:31	60196.296	$(1.67^{+0.12}_{-0.13}) \times 10^{38}$	$(4.0 \pm 0.4) \times 10^{30}$	-0.018 ± 0.014	5.50
2023-09-14T02:59:42	60201.125	$(1.58^{+0.15}_{-0.15}) \times 10^{38}$	$(3.8 \pm 0.4) \times 10^{30}$	$+0.075 \pm 0.001$	4.75
2023-09-15T23:47:11	60202.991	$(1.66^{+0.13}_{-0.13}) \times 10^{38}$	$(3.9 \pm 0.4) \times 10^{30}$	$+0.062 \pm 0.072$	5.20
2023-09-16T15:30:40	60203.646	$(1.68^{+0.16}_{-0.16}) \times 10^{38}$	$(4.0 \pm 0.4) \times 10^{30}$	$+0.108 \pm 0.001$	1.28
2023-09-17T02:29:36	60204.104	$(1.61^{+0.12}_{-0.12}) \times 10^{38}$	$(3.9 \pm 0.4) \times 10^{30}$	$+0.108 \pm 0.001$	5.75
2024-03-21T21:45:25	60390.907	$(2.22^{+0.15}_{-0.16}) \times 10^{36}$	$(4.2 \pm 0.5) \times 10^{28}$	$+0.2 \pm 0.3$	5.50
2024-03-24T00:52:42	60393.037	$(2.01^{+0.14}_{-0.15}) \times 10^{36}$	$(4.7 \pm 0.7) \times 10^{28}$	$+0.12 \pm 0.07$	5.50
2024-03-24T21:54:30	60393.913	$(1.95^{+0.14}_{-0.14}) \times 10^{36}$	$(4.5 \pm 0.5) \times 10^{28}$	$+0.12 \pm 0.07$	1.28
2024-03-27T00:45:35	60396.032	$(1.80^{+0.13}_{-0.14}) \times 10^{36}$	$(4.6 \pm 0.9) \times 10^{28}$	$+0.02 \pm 0.08$	5.50
2024-03-30T23:48:29	60399.992	$(1.55^{+0.13}_{-0.13}) \times 10^{36}$	$(4.4 \pm 0.6) \times 10^{28}$	$+0.04 \pm 0.07$	6.22
2024-03-31T17:09:30	60400.715	$(1.51^{+0.13}_{-0.13}) \times 10^{36}$	$(4.4 \pm 0.4) \times 10^{28}$	$+0.04 \pm 0.07$	1.28
2024-04-06T12:01:02	60406.501	$(1.14^{+0.09}_{-0.09}) \times 10^{36}$	$(2.0 \pm 0.2) \times 10^{28}$	-0.17 ± 0.09	1.28
2024-04-07T22:16:08	60407.928	$(1.05^{+0.10}_{-0.10}) \times 10^{36}$	$(1.8 \pm 0.3) \times 10^{28}$	-0.17 ± 0.09	6.22
2024-04-12T23:27:14	60412.977	$(8.6^{+0.7}_{-0.8}) \times 10^{35}$	$(1.5 \pm 0.3) \times 10^{28}$	-0.17 ± 0.1	6.22
2024-04-13T12:54:07	60413.538	$(8.4^{+0.8}_{-0.8}) \times 10^{35}$	$(1.44 \pm 0.15) \times 10^{28}$	-0.17 ± 0.1	1.28
2024-04-20T07:56:32	60420.331	$(5.9^{+0.6}_{-0.6}) \times 10^{35}$	$(1.04 \pm 0.12) \times 10^{28}$	-0.28 ± 0.09	1.28
2024-04-21T22:31:32	60421.939	$(5.5^{+0.4}_{-0.4}) \times 10^{35}$	$(9.99 \pm 0.18) \times 10^{27}$	-0.28 ± 0.09	1.28
2024-04-28T23:41:07	60428.987	$(1.10^{+0.10}_{-0.10}) \times 10^{35}$	$(6.89 \pm 0.13) \times 10^{27}$	-0.28 ± 0.09	6.22
2024-05-05T21:26:16	60435.893	$(6.2^{+0.7}_{-0.7}) \times 10^{33}$	$(2.6 \pm 0.8) \times 10^{27}$	-0.60 ± 0.17	1.28
2024-05-08T07:00:37	60438.292	$(2.1^{+0.3}_{-0.3}) \times 10^{33}$	$(2.0 \pm 0.4) \times 10^{27}$	-0.60 ± 0.17	3.06
2024-05-11T21:47:40	60441.908	$(7^{+5}_{-3}) \times 10^{32}$	$(8.0 \pm 0.4) \times 10^{26}$	-1.0 ± 0.3	6.22
2024-05-13T21:32:47	60443.898	$(6^{+4}_{-3}) \times 10^{32}$	$(9.8 \pm 0.3) \times 10^{26}$	-1.0 ± 0.3	1.28
2024-05-14T09:44:32	60444.406	$(6^{+3}_{-2}) \times 10^{32}$	$(7.7 \pm 0.3) \times 10^{26}$	-1.0 ± 0.3	6.22
2024-05-18T22:20:57	60448.931	$(5^{+1.6}_{-1.3}) \times 10^{32}$	$(1.5 \pm 0.5) \times 10^{27}$	-0.6 ± 0.2	1.28
2024-05-23T05:51:22	60453.244	$(3.0^{+1.1}_{-0.8}) \times 10^{32}$	$(1.2 \pm 0.3) \times 10^{27}$	-0.6 ± 0.2	6.22
2024-05-25T22:10:15	60455.924	$(1.5^{+1.6}_{-0.7}) \times 10^{32}$	$(1.1 \pm 0.4) \times 10^{27}$	-0.6 ± 0.2	1.28
2024-05-29T10:54:34	60459.455	$(9.0^{+8}_{-4}) \times 10^{31}$	$(3 \pm 2) \times 10^{26}$	-0.6 ± 0.2	6.00

Table C1. Summary of radio and X-ray properties presented in Figure 1 (assuming $D=2.6$ kpc). Columns list the observation date (UTC), Modified Julian Date (MJD), X-ray luminosity in the 1–10 keV band (L_X), interpolated onto the radio observing epochs, radio luminosity at 5 GHz (L_R), radio spectral index (α), and the observing radio frequency (ν_{obs}). X-ray luminosities are based on *Swift*-XRT data, and radio values are extrapolated to 5 GHz assuming the listed spectral indices. The top section corresponds to the rise hard state; the bottom, the decay hard state. Uncertainties represent 1σ errors.